Biomech Model Mechanobiol (2010) 9:127–139
DOI 10.1007/s10237-009-0163-4

ORIGINAL PAPER

Evaluating patient-specific abdominal aortic aneurysm wall stress based on flow-induced loading

A. Dorfmann · C. Wilson · E. S. Edgar · R. A. Peattie

Received: 27 February 2009 / Accepted: 16 June 2009 / Published online: 4 July 2009

Abstract In this paper, we develop a physiologic wall stress analysis procedure by incorporating experimentally measured, non-uniform pressure loading in a patient-based finite element simulation. First, the distribution of wall pressure is measured in a patient-based lumen cast at a series of physiologically relevant steady flow rates. Then, using published equi-biaxial stress-deformation data from aneurysmal tissue samples, a nonlinear hyperelastic constitutive equation is used to describe the mechanical behavior of the aneurysm wall. The model accounts of the characteristic exponential stiffening due to the rapid engagement of nearly inextensible collagen fibers and assumes, as a first approximation, an isotropic behavior of the arterial wall. The results show a complex wall stress distribution with a localized maximum principal stress value of 660 kPa on the inner surface of the posterior surface of the aneurysm bulge, a considerably larger value than has generally been reported in calculations of wall stress under the assumption of uniform loading. This is potentially significant since the posterior wall has been suggested as a common site of rupture, and the aneurysmal tensile strength reported by other authors is of the same order of magnitude as the maximum stress value found here.

A. Dorfmann (✉) · C. Wilson
Department of Civil and Environmental Engineering,
Tufts University, Medford, MA 02155, USA
e-mail: luis.dorfmann@tufts.edu

E. S. Edgar
Department of Chemical Engineering, Oregon State University,
Corvallis, OR 97331, USA

R. A. Peattie
Department of Biomedical Engineering, Tufts University,
Medford, MA 02155, USA

Keywords Abdominal aortic aneurysms · Non-uniform wall pressure distribution · Patient-specific analysis · Flow field measurements

1 Introduction

Abdominal aortic aneurysms (AAAs) represent permanent localized expansions of the aorta that form between the renal arteries and the iliac bifurcation. Their prevalence increases with age, and it has been estimated that they may occur in as many as 9% of males over 65 (Newman et al. 2001; Singh et al. 2001). Since AAAs form at regions in which the vessel wall is diseased and weakened, they are at risk of rupture. Johansson and Swedenborg (1986) report that mortality associated with AAA rupture can exceed 90%, accounting for 15,000 deaths annually in the U.S. alone (National Center for Health Statistics 2008, http://www.cdc.gov/nchs/deaths.htm), making AAA ruptures the 13th leading cause of death in western societies. Although AAAs can be surgically repaired by either open-abdomen or endovascular approaches if diagnosed, those procedures have their own risks. Hence clinical decisions concerning AAA management are normally made balancing the risks associated with surgical intervention against the risk of eventual lesion rupture.

Unfortunately, there does not yet exist a quantitatively accurate method for assessing failure likelihood for specific AAA patients. Current clinical practice is to evaluate the likelihood of rupture only on the basis of the maximum transverse bulge diameter, ignoring all other factors that contribute to failure. Nevitt et al. (1989) and Ashton et al. (2002) have suggested that failure probability is significantly increased when bulge diameter exceeds 5 cm. However, Darling et al. (1977) have shown that even lesions <4 cm can fail with significant

frequency. Moreover, from a biomechanical standpoint, internal stress is the physical factor that causes wall failure, not wall diameter. Accordingly, rupture can be expected to be increasingly likely as the wall stresses generated by flow-induced hemodynamic forces approach or exceed the strength of the diseased wall. In addition, local geometric factors other than diameter can be expected to alter flow field properties and lead to local stress concentrations that increase the probability of failure, while wall material property variations can alter the wall's ability to support those stresses. Thus an accurate method for predicting risk of rupture for specific patients should properly be based on quantitative understanding of the relations between the evolution of flow fields within the lesions of those patients and the resulting wall stress development.

Although no valid technique for measuring wall stress non-invasively in vivo has been developed yet, techniques for modeling wall stress on a patient-specific basis have evolved rapidly in the last few years, representative publications being the papers by Speelman et al. (2007), Vande Geest et al. (2008), Li et al. (2008) and Rodríguez et al. (2008). Recent reviews articles are the papers by Fillinger (2006), Vorp (2007) and Humphrey and Taylor (2008). Broadly speaking, efforts to model wall stress can be categorized into two groups, (i) static and quasi-static finite element wall-only models in which no account is taken of flow within the lesion other than to assume pressure is constant along the wall inner surface and (ii) fluid–structure interaction (FSI) calculations in which a large computational package is used to compute the flow field and resulting wall stress distribution simultaneously. Efforts to perform finite element wall stress analyzes in patient-based models were introduced by Raghavan and Vorp (2000) and Raghavan et al. (2000), and have evolved rapidly in complexity from initial isotropic material models to recent studies incorporating anisotropic behavior, non-uniform thrombus distribution and wall calcifications (Raghavan and Vorp 2000; Vande Geest 2005; Vande Geest et al. 2004, 2008; Wang et al. 2002; Speelman et al. 2007). Maximum principal stress values and directions have been found to be highly dependent on the specific shape and thrombus distribution of the patient lesion and the material behavior emulated in the calculation, though values in the range of 400–750 kPa are typical. Generally consistent results have been reported by Speelman et al. (2007), Truijers et al. (2007), Vande Geest et al. (2008) and Li et al. (2008), with maximum stress values dependent on the specific model details.

A significant limitation of these methods, though, is that patient-based finite element calculations to date have relied on the assumption that the wall is subject only to uniform internal loading at constant pressure, normally a peak systolic of 16 kPa. FSI computations (Li and Kleinstreuer 2006; Papaharilaou et al. 2007; Scotti et al. 2008; Bluestein et al. 2009; Rissland et al. 2009) avoid this assumption, by calculating an intraluminal flow field and allowing non-uniform wall pressure to be elicited by the flow. However, all published FSI computations to date have assumed the flow field to be laminar. Unfortunately, it has been shown repeatedly in vivo and in vitro, in idealized and patient-based phantoms, under steady and pulsatile conditions, that AAA flow fields are usually highly non-laminar. Results published on this topic are described in the papers by Bluth et al. (1990), Asbury et al. (1995), Peattie et al. (2004, 1996a,b) and O'Rourke and McCullough (2008). Thus there remains the need for an analysis approach that calculates wall stress based on loading that replicates in vivo conditions, and incorporates the effects of wall loading when the flow is unstable.

In the present paper, we describe an initial attempt to develop a physiologic wall stress analysis procedure; that is, a finite element computational technique that evaluates the wall stress distribution and maxima in models accurately replicating the shape of individual AAA patient lesions and incorporating published wall material properties, but using load distributions derived from wall pressure measurements in corresponding experimental phantoms. As flow rate varies, the flow field may be either laminar or turbulent. In either case, the flow-induced wall pressure distribution reflects the flow field, and may or may not be stable or show nearly uniform magnitude depending on the patient geometry and flow rate. We show that the measured wall pressure distribution can be applied as loading condition for a finite element wall stress calculation, and the resulting wall stress field can be quantitatively characterized in detail.

2 Experiments

2.1 Methods

All procedures were carried out with full approval from the Institutional Review Boards of Hartford Hospital and Tufts University. The AAA models were developed from a AAA patient CT image series performed at Hartford Hospital (Hartford, CT) using a spiral CT imaging system (Model 9800 High Speed Scanner, General Electric Healthcare Inc.), with a nominal slice thickness of 0.6 mm and a helical pitch of 1.5 : 1. Images were obtained from one end of the abdomen to the other during a single sustained breath hold by the patient to minimize respiratory-induced artifacts, after intravenous administration of standard non-ionic contrast enhancement agent.

Commercial software (*MIMICS* V9.0, Materialise Inc.) was used to create the three-dimensional representation of the AAA lumen, which is shown in Fig. 1. Initially, the CT series contained segments of the non-dilated aorta both proximal and distal to the bulge, as well as the iliac bifurcation

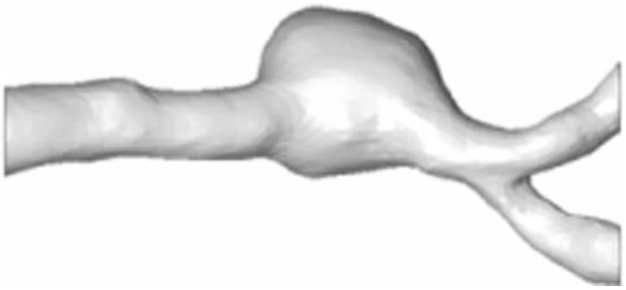

Fig. 1 Three-dimensional solid model of the patient-specific AAA lumen with non-dilated inner diameter of 23.2 mm, maximum bulge outer diameter of 56.5 mm and bulge length of 67 mm

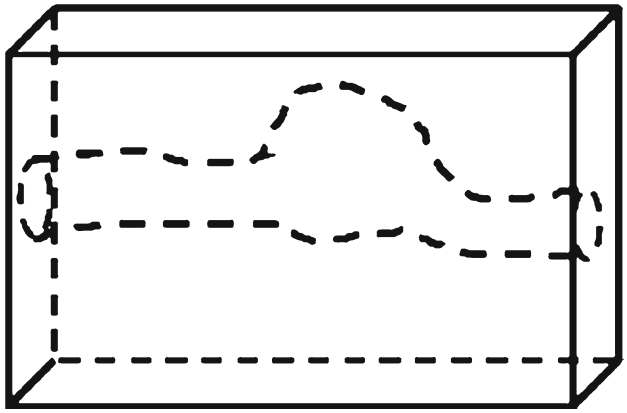

Fig. 2 Benchtop phantom replicating the diseased aortic lumen

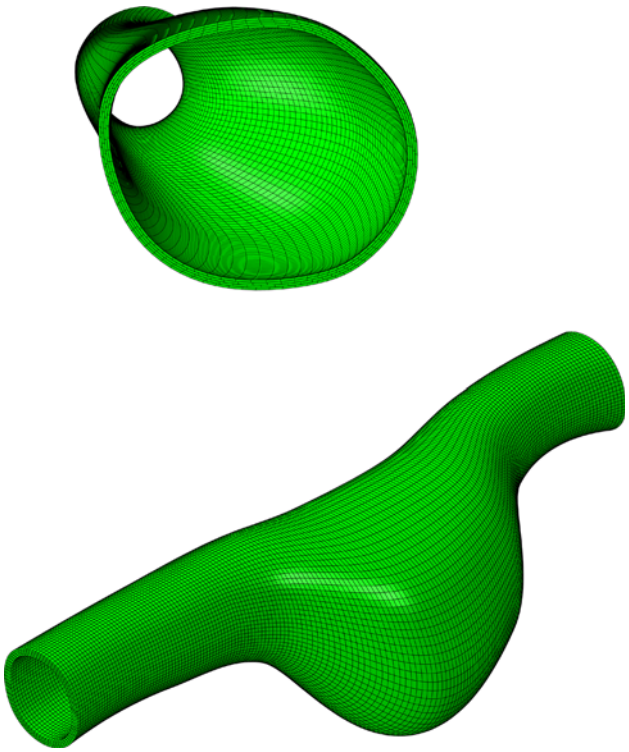

Fig. 3 Geometric layout and element distribution of the finite element model used to compute wall stress distributions. The model uses a total of 63,654 elements connected at 127,926 nodes. Four hexahedron elements are used through the wall thickness

and short segments of each common iliac artery. However, to facilitate installation in a flow loop, prior to model construction it was terminated proximally at the plane of the *T* 11 vertebra and distally one diameter downstream of the bulge, leaving an entrance length of approximately four aorta diameters upstream of the bulge. Branch arteries were trimmed from it as well. The result was a single curved, bulged but unbranched vessel, of non-dilated aortic diameter 2.3 cm, maximum bulge lumen diameter 5.5 cm and bulge length 6.7 cm. The magnitude of the principal geometric dimensions are listed in Table 1 and a full description of the lumen is given by Edgar (2008).

Two types of models were created from the imaging. The first, a benchtop phantom replicating the diseased aortic lumen, is schematically shown in Fig. 2. The second, shown in Fig. 3, is the computational model of the arterial wall for finite element analysis. Methods for constructing the phantom and its use in a flow loop are described in detail by Edgar (2008). In brief, a solid polymeric construct of the lumen was fabricated by stereolitography, then replicated in wax. The wax replica was then suspended in a polished casting jig and an elastomer (Sylgard 184, Dow Corning, Midland, MI) poured around it. When the elastomer had cured, the wax was dissolved away, leaving a clear, effectively rigid, flow-through cast whose interior precisely replicated the desired lumenal shape.

Steady flow was delivered through the phantom by a constant head, gravitationally driven flow loop schematically shown in Fig. 4. Experiments were conducted at a series of flow rates between 0.3 and 1.5 L/min, producing Reynolds numbers from 500 to 3000, the operating range of the abdominal aorta under conditions from rest to exercise (Fung 1981). To ensure the flow field was fully developed at the measurement locations, 1.5 m lengths of straight, rigid tubing were positioned in the flow loop immediately up- and

Table 1 Magnitudes and dimensions of geometric model parameters

d (cm)	D_{AAA} (cm)	D_{l} (cm)	L_{AAA} (cm)	V_{AAA} (cm)	V_{Th} (ml)	κ (cm^{-1})	T
2.32	5.65	5.50	6.70	135.1	0	0.453	1.38

d non-dilated vessel inner diameter, D_{AAA} maximum bulge outer diameter, D_l maximum lumen diameter, L_{AAA} bulge length, V_{AAA} bulge volume, V_{Th} mural thrombus volume, κ maximum bulge curvature, T tortuosity

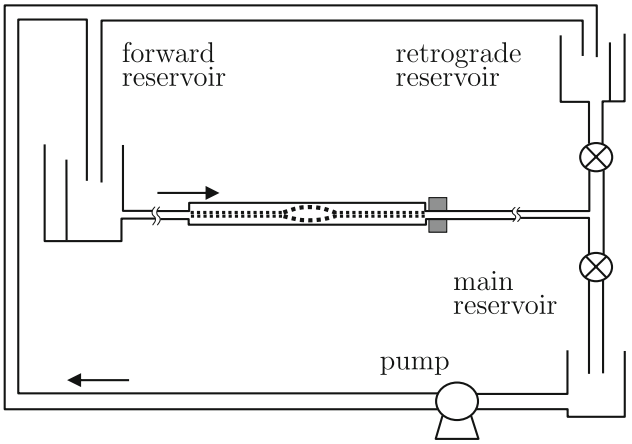

Fig. 4 Schematic diagram of the flow loop, showing the positions of the model, the reservoirs and the control valves. Flow in the forward direction refers to proximal-to-distal motion from the forward reservoir, while retrograde motion is the reverse

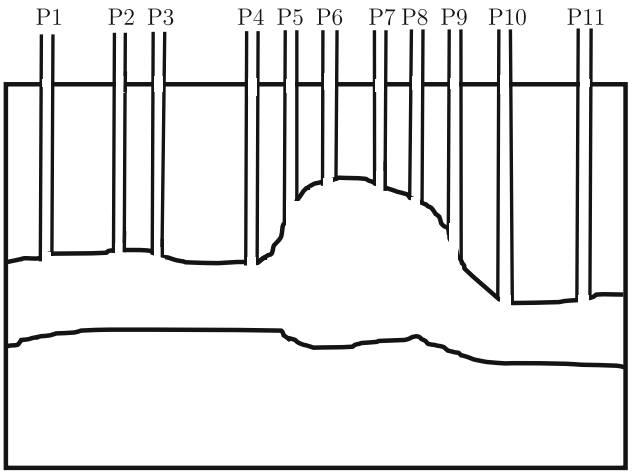

Fig. 5 Pressure tap positions in the phantom

downstream of the phantom. The working fluid of these experiments was tap water. Reynolds numbers were calculated as $Re = 4Q/\pi\nu d$, where Q is volume flow rate, ν is kinematic viscosity and d is the diameter of the non-dilated entrance tube proximal to the bulge.

The pressure distribution along the phantom wall was measured at eleven 3 mm taps drilled through the wall and connected to pressure transducers (Utah Medical Products Inc., model DPT-400), see Fig. 5. The noise-limited resolution of these transducers was measured in situ in both the presence and absence of flow, and was found to vary between 0.1 and 0.15 mmHg, depending on flow rate. Output from the transducers was obtained from a four-channel monitor (Hewlett-Packard Inc., model 78532B). The transducers were calibrated by applying a set of known hydrostatic pressures via a column of water prior to making measurements.

Measurements were first corrected to account for the vertical distance of the transducers above the bulge surface. Raw wall pressure values were then decomposed into the sum of hydrostatic and dynamic components. Each term was separately re-scaled to reflect in vivo conditions, based on the density of blood and on the dynamic pressure ($0.5\rho U^2$) where ρ is the density and $U = 4Q/\pi d^2$ is the mean velocity in the entrance tube. The terms were then re-combined, so that the pressure values presented represent in vivo values.

Pressure was recorded at each station at a series of steady flow rates between 0.3 and 1.5 L/min, producing Reynolds numbers from 500 to 3000. At flow rates below $Re = 1500$, the pressure signal at each transducer was steady, so that direct readings were sufficient. As the flow rate increased beyond $Re = 1500$, however, the pressure signal became progressively unstable and fluctuated randomly. Separate velocity measurements showed the flow to be very unstable and to break down into turbulence at these high flow rates. Both the time-average and standard deviation of the pressure signal were then determined.

2.2 Results

Only the mean pressure at each station at $Re = 3000$ was used for subsequent calculations. Figure 6 presents the mean $\pm$ standard deviation of the pressure distribution at this Re, curve fitted by least squares regression for subsequent computation purposes. Wall pressure was greatest at the phantom entrance (16.0 kPa at $x = 0$, where x is axial position measured from the phantom entrance), dipped to a minimum of 15.5 kPa at the mid-bulge (x = 120–140 mm), then recovered to 15.9 kPa at the bulge exit ($x = 215$ mm). The overall

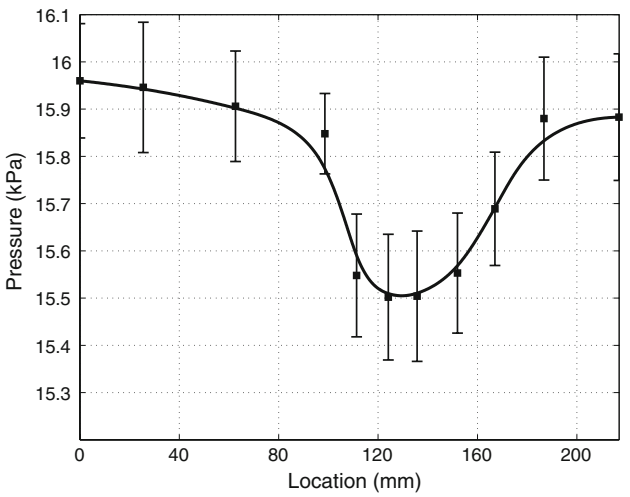

Fig. 6 Mean pressure $\pm$ standard deviation at $Re = 3000$ at each measurement station. Curve fitted by least squares regression for subsequent computation purposes

pressure drop along the phantom was therefore 0.1 kPa, and the associated pressure gradient was sufficient to produce a net flow rate of $Re = 3000$. Although the pressure drop in the middle of the bulge was surprising, it was found repeatably for all Reynolds numbers. Presumably, it results from the combination of hydrostatic and inertial effects in the fluid and the curvature of the phantom axis. Standard deviations of the pressure values reflect the instability of the measurements. They are an order of magnitude larger than the noise-limited resolution of the transducers, and presumably result from the effects of flow turbulence.

For test purposes, the pressure distribution shown in Fig. 6 was used as loading for subsequent calculation of wall stress distribution. A control case with uniform $p = 16\,\text{kPa}$ was also calculated.

3 Basic equations

In this section, we provide a brief overview of the nonlinear theory of elasticity, which is of fundamental importance to describe the resulting finite deformations of soft biological tissues in general and the arterial response in particular. Note, that in this analysis we focus merely on the *isotropic mechanical behavior* and do not account of preferred directions attributed to the presence of collagen fibers. Also, we do not separately include the mechanical characteristics of the three individual arterial layers but focus on the macroscopic behavior of the arterial wall. We account of finite deformation, highly nonlinear stress–strain response and exponential stiffening at high pressures. For a detailed discussion of the mechanical response of individual layers of the arterial wall, including anisotropic constitutive laws, we refer to Holzapfel et al. (2000). The main emphasis of this work is to use, for the first time, an experimentally determined flow-induced wall pressure distribution to evaluate the wall stress in a patient-based aneurysm model.

3.1 Kinematics

To describe the deformation, we denote the stress-free reference configuration by $\mathcal{B}_r$ and identify a generic material point by its position vector $\mathbf{X}$ relative to an arbitrary chosen origin. Application of mechanical forces deforms the body, so that the point $\mathbf{X}$ occupies the new position $\mathbf{x} = \boldsymbol{\chi}(\mathbf{X})$ in the deformed configuration $\mathcal{B}$. The vector field $\boldsymbol{\chi}$ describes the deformation of the body and assigns to each point $\mathbf{X}$ a unique position $\mathbf{x}$ in $\mathcal{B}$ and viceversa attributes a unique reference position $\mathbf{X}$ in $\mathcal{B}_r$ to each point $\mathbf{x}$. In other words, the deformation function $\boldsymbol{\chi}$ is a one-to-one mapping with suitable regularity properties.

The deformation gradient tensor $\mathbf{F}$ relative to $\mathcal{B}_r$, is defined by

$$\mathbf{F} = \text{Grad}\,\mathbf{x}, \tag{1}$$

Grad being the gradient operator with respect to $\mathbf{X}$. The Cartesian components are $F_{i\alpha} = \partial x_i/\partial X_\alpha$, where x_i and X_α are the components of $\mathbf{x}$ and $\mathbf{X}$, respectively, with $i, \alpha \in \{1, 2, 3\}$. Roman indices are associated with $\mathcal{B}$ and Greek indices with $\mathcal{B}_r$. We also adopt the standard notation

$$J = \det \mathbf{F} = \frac{\mathrm{d}v}{\mathrm{d}V} > 0. \tag{2}$$

The deformation gradient can be decomposed according to the unique polar decomposition

$$\mathbf{F} = \mathbf{RU} = \mathbf{VR}, \tag{3}$$

where $\mathbf{R}$ is a proper orthogonal tensor and $\mathbf{U}$ and $\mathbf{V}$ are positive definite and symmetric, respectively, the right and left stretch tensors. These can be expressed in spectral form. For $\mathbf{U}$, for example, we have the spectral decomposition

$$\mathbf{U} = \sum_{i=1}^{3} \lambda_i \mathbf{u}^{(i)} \otimes \mathbf{u}^{(i)}, \tag{4}$$

where the principal stretches $\lambda_i > 0$, $i \in \{1, 2, 3\}$, are the eigenvalues of $\mathbf{U}$, $\mathbf{u}^{(i)}$ are the (unit) eigenvectors of $\mathbf{U}$, and $\otimes$ denotes the tensor product. For an incompressible material, which is a typical assumption for biomaterials, we have

$$J = \det \mathbf{F} = \det \mathbf{U} = \det \mathbf{V} = \lambda_1\lambda_2\lambda_3 \equiv 1. \tag{5}$$

Using the polar decomposition (3), we define

$$\mathbf{C} = \mathbf{F}^{\mathrm{T}}\mathbf{F} = \mathbf{U}^2, \quad \mathbf{B} = \mathbf{F}\mathbf{F}^{\mathrm{T}} = \mathbf{V}^2, \tag{6}$$

which denote the right and left Cauchy–Green deformation tensors, respectively.

The three principal invariants for $\mathbf{C}$, equivalently $\mathbf{B}$, are defined by

$$I_1 = \text{tr}\,\mathbf{C}, \quad I_2 = \frac{1}{2}\left[(\text{tr}\,\mathbf{C})^2 - \text{tr}\,(\mathbf{C}^2)\right], \quad I_3 = \det \mathbf{C} = J^2, \tag{7}$$

where tr is the trace of a second-order tensor. Recall that for an incompressible material the third invariant $I_3 \equiv 1$. Alternatively, in terms of principal stretches, the invariants I_1, I_2, I_3 are expressed as

$$I_1 = \lambda_1^2 + \lambda_2^2 + \lambda_3^2, \quad I_2 = \lambda_1^2\lambda_2^2 + \lambda_2^2\lambda_3^2 + \lambda_3^2\lambda_1^2, \quad I_3 = \lambda_1^2\lambda_2^2\lambda_3^2. \tag{8}$$

For full details of the kinematics of solid continua we refer to, for example, Ogden (1997) and Holzapfel (2001).

3.2 Hyperelasticity

The theory of hyperelasticity characterizes the elastic response of a material by a strain energy function W defined per unit volume in the reference configuration $\mathcal{B}_r$. For a homogeneous material W depends only on the deformation gradient $\mathbf{F}$ and we write $W = W(\mathbf{F})$. For an incompressible material, the nominal stress tensor $\mathbf{S}$ and the symmetric Cauchy stress tensor $\boldsymbol{\sigma}$ are given in terms of W, respectively, by

$$\mathbf{S} = \frac{\partial W}{\partial \mathbf{F}} - p\mathbf{F}^{-1}, \quad \boldsymbol{\sigma} = \mathbf{F}\frac{\partial W}{\partial \mathbf{F}} - p\mathbf{I}, \tag{9}$$

where $\mathbf{I}$ is the identity tensor and p an arbitrary hydrostatic pressure. Equation (9) shows that for an incompressible material, the Cauchy stress $\boldsymbol{\sigma}$ and the nominal stress $\mathbf{S}$ are related by $\boldsymbol{\sigma} = \mathbf{FS}$.

According to the principle of objectivity, W depends on $\mathbf{F}$ through $\mathbf{U}$ and we write

$$W(\mathbf{F}) = W(\mathbf{U}). \tag{10}$$

This allows to introduction of the symmetric stress tensor $\mathbf{T}$ defined by

$$\mathbf{T} = \frac{\partial W}{\partial \mathbf{U}} - p\mathbf{U}^{-1}, \quad \det \mathbf{U} = 1, \tag{11}$$

known as Biot stress tensor. If the strain energy formulation is expressed in terms of $\mathbf{U}$, the objectivity requirement is automatically satisfied.

3.2.1 Isotropic hyperelasticity

For an *isotropic* elastic solid W depends on the deformation only through the principal invariants defined by Eq. (7), we write $W = W(I_1, I_2, I_3)$. In order to obtain explicit expressions of the nominal stress tensor $\mathbf{S}$ and the associated Cauchy stress tensor $\boldsymbol{\sigma}$, the derivatives of the strain invariants with respect to $\mathbf{F}$ are needed. Following standard derivation rules, these are given by

$$\begin{aligned} &\frac{\partial I_1}{\partial \mathbf{F}} = 2\mathbf{F}^{\mathrm{T}}, \quad \frac{\partial I_2}{\partial \mathbf{F}} = 2(I_1\mathbf{F}^{\mathrm{T}} - \mathbf{F}^{\mathrm{T}}\mathbf{F}\mathbf{F}^{\mathrm{T}}), \\ &\frac{\partial I_3}{\partial \mathbf{F}} = 2I_3\mathbf{F}^{-1}. \end{aligned} \tag{12}$$

For an incompressible material $I_3 = 1$ and only two invariants are needed. These are I_1 and I_2 and the strain energy function can be written in the form $W = W(I_1, I_2)$. A direct calculation of the Eqs. (9), using the results shown in (12), leads to

$$\mathbf{S} = 2(W_1 + I_1 W_2)\mathbf{F}^{\mathrm{T}} - 2W_2\mathbf{C}\,\mathbf{F}^{\mathrm{T}} - p\,\mathbf{F}^{-1}, \tag{13}$$

and

$$\boldsymbol{\sigma} = 2(W_1 + I_1 W_2)\mathbf{B} - 2W_2\mathbf{B}^2 - p\,\mathbf{I}, \tag{14}$$

where the notation $W_i = \partial W/\partial I_i$ with $i \in \{1, 2\}$ has been introduced.

Equivalently, we may regard W as a symmetric function of the principal stretches $\lambda_1, \lambda_2, \lambda_3$. We write this dependence as

$$W(\lambda_1, \lambda_2, \lambda_3) = W(\lambda_2, \lambda_3, \lambda_1) = W(\lambda_3, \lambda_1, \lambda_2). \tag{15}$$

Consequences of isotropy are that $\mathbf{S} = \mathbf{T}\mathbf{R}^T$ and that $\mathbf{T}$ is coaxial with $\mathbf{U}$. Thus, similarly to (4), we have

$$\mathbf{T} = \sum_{i=1}^{3} t_i \mathbf{u}^{(i)} \otimes \mathbf{u}^{(i)}, \tag{16}$$

where t_i, $i \in \{1, 2, 3\}$, are the principal Biot stresses, given by

$$t_i = \frac{\partial W}{\partial \lambda_i} - p\lambda_i^{-1}, \quad \lambda_1\lambda_2\lambda_3 = 1. \tag{17}$$

The principal Cauchy stresses σ_i, $i \in \{1, 2, 3\}$ for an incompressible material are

$$\sigma_i = \lambda_i \frac{\partial W}{\partial \lambda_i} - p. \tag{18}$$

3.2.2 Application to homogeneous biaxial deformations

In this subsection, we apply the theory described above to the problem of homogeneous biaxial deformations. On use of the incompressibility constraint (5), the strain–energy function (15) can be written in terms of two independent stretches in the form

$$\hat{W}(\lambda_1, \lambda_2) = W(\lambda_1, \lambda_2, \lambda_1^{-1}\lambda_2^{-1}), \tag{19}$$

which is symmetric in λ_1 and λ_2. Then, from (18), after eliminating the pressure p, we obtain the Cauchy stress differences

$$\sigma_1 - \sigma_3 = \lambda_1 \frac{\partial \hat{W}}{\partial \lambda_1}, \quad \sigma_2 - \sigma_3 = \lambda_1 \frac{\partial \hat{W}}{\partial \lambda_2}. \tag{20}$$

Equations (20) provide a basis for characterizing the form of the energy function using biaxial tests in which λ_1 and λ_2 are varied independently, for more detail we refer to Holzapfel and Ogden (2009). For this purpose and without loss of generality we can set σ_3 equal to zero so that, in particular, Eqs. (20) become

$$\sigma_1 = \lambda_1 t_1 = \lambda_1 \frac{\partial \hat{W}}{\partial \lambda_1}, \quad \sigma_2 = \lambda_2 t_2 = \lambda_2 \frac{\partial \hat{W}}{\partial \lambda_2}. \tag{21}$$

Accurate determination of material model parameters included in $\hat{W}(\lambda_1, \lambda_2)$ requires use of (21) with t_1 and t_2 measured for given pairs of values of λ_1 and λ_2.

3.2.3 Simple tension and compression

In the simple tension (or compression) specialization we take $\lambda_2 = \lambda_3$, and we use the notation

$$\lambda_1 = \lambda, \quad \lambda_2 = \lambda^{-1/2}. \tag{22}$$

The strain energy then depends on the one remaining independent stretch, and we write

$$\tilde{W}(\lambda) = \hat{W}(\lambda, \lambda^{-1/2}). \tag{23}$$

In this case $\sigma_2 = \sigma_3 = 0$ and the Cauchy and nominal (or Biot) stresses associated with λ_1 are, respectively,

$$\sigma = \sigma_1 = \lambda \frac{\mathrm{d}\tilde{W}(\lambda)}{\mathrm{d}\lambda}, \quad t = \frac{\sigma}{\lambda} = \frac{\mathrm{d}\tilde{W}(\lambda)}{\mathrm{d}\lambda}. \tag{24}$$

4 Constitutive model

An arterial wall has residual stresses in the load-free configuration and is known to be anisotropic due to the presence of embedded collagen fibers. Appropriate constitutive laws have been developed to account for the rather complicated structure. In this study, however, as a first approximation, we assume the mechanical response of the arterial wall to be isotropic. The rapid stiffening, when large loads are applied, can best be described by a constitutive model based on an exponential strain energy formulation. Following Demiray (1972), Humphrey and Yin (1987), Rodríguez et al. (2008) and Lin et al. (2009), amongst many others, we propose the simple I_1 function in the form

$$W = \frac{\mu}{2\alpha}\{\exp[\alpha(I_1 - 3)] - 1\}, \tag{25}$$

where μ is the shear modulus of the material in the reference configuration, α is a positive parameter both to be determined from experimental data. Note, that in the limit for $\alpha \to 0$ the strain energy formulation (25) becomes the classical neo-Hookean model.

Biological materials, including arterial walls, are assumed to be almost incompressible for the physiological range of deformations (Chuong and Fung 1984; Holzapfel et al. 2000). Using Eq. (14) the Cauchy stress tensor becomes

$$\boldsymbol{\sigma} = \mu\{\exp[\alpha(I_1 - 3)]\mathbf{B}\} - p\mathbf{I}\}, \tag{26}$$

and in component form

$$\sigma_{ij} = \mu\{\exp[\alpha(I_1 - 3)]B_{ij}\} - p\delta_{ij}, \tag{27}$$

where B_{ij} are the components of the left Cauchy–Green tensor. In the absence of mechanical body forces, the Cauchy stress tensor must satisfy the equilibrium equation

$$\mathrm{div}\,\boldsymbol{\sigma} = \mathbf{0}. \tag{28}$$

together with properly posed boundary conditions.

4.1 Homogenous biaxial deformation

In this subsection the constitutive equation is applied to basic deformation, known as pure homogeneous strain and given by

$$x_1 = \lambda_1 X_1, \quad x_2 = \lambda_2 X_2, \quad x_3 = \lambda_3 X_3, \tag{29}$$

where the principal stretches λ_1, λ_2 and λ_3 are constants. The Cartesian coordinates in the reference configuration are denoted (X_1, X_2, X_3) and in the deformed configuration (x_1, x_2, x_3). For a planar biaxial deformation the gradient $\mathbf{F} = \mathbf{U}$ and the principal axes of deformation coincide with the Cartesian coordinate directions.

Consider a thin square specimen of an arterial wall that lies in the (X_1, X_2)-plane and free to deform in the X_3-direction. For incompressible materials we have $\lambda_1\lambda_2\lambda_3 = 1$, which implies that only two of the stretches are independent, i.e. $\lambda_3 = \lambda_1^{-1}\lambda_2^{-2}$. Therefore, for the planar biaxial deformation the invariant I_1 becomes

$$I_1 = \lambda_1^2 + \lambda_2^2 + \lambda_1^{-2}\lambda_2^{-2}. \tag{30}$$

The principal in-plane stresses are then obtained from (21) as

$$\begin{aligned} \sigma_1 &= \mu(\lambda_1^2 - \lambda_1^{-2}\lambda_2^{-2})\exp[\alpha(I_1 - 3)], \\ \sigma_2 &= \mu(\lambda_2^2 - \lambda_1^{-2}\lambda_2^{-2})\exp[\alpha(I_1 - 3)], \end{aligned} \tag{31}$$

with all remaining stress components equal zero.

4.2 Simple tension

As in Sect. 3.2.3, for simple tension we take $\sigma_2 = \sigma_3 = 0$ and write $\sigma_1 = \sigma$. We also write $\lambda_1 = \lambda$, so that $\lambda_2 = \lambda_3 = \lambda^{-1/2}$, and define $\tilde{W}$ by

$$\tilde{W}(\lambda) = \hat{W}(\lambda, \lambda^{-1/2}). \tag{32}$$

On the basis of Eq. $(24)_1$, the Cauchy stress component for simple tension is

$$\sigma = \mu(\lambda^2 - \lambda^{-1})\exp[\alpha(I_1 - 3)] \tag{33}$$

with $I_1 = \lambda^2 - 2\lambda^{-1}$.

4.3 Anisotropy and residual stresses

The constitutive law considered thus far does not account for the markedly anisotropic behavior of arterial tissues arising from the recruitment of collagen fibers for increasing wall pressures and from the residual stress distribution in the load-free configuration. It is well known that the degree of anisotropy depends on the magnitude of applied load and the amount of pre-stretch, i.e. it is specified with respect

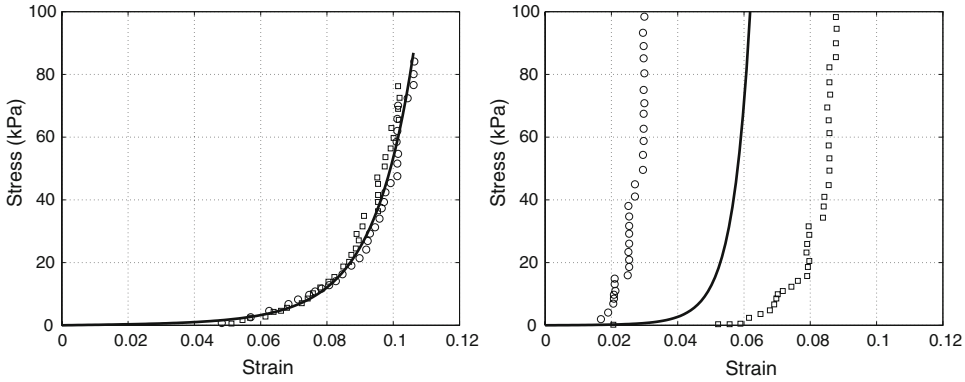

Fig. 7 Equi-biaxial data of healthy abdominal aortic specimen on the *left*, and of an AAA specimen on the *right*. The symbols *open circle* and *open square* indicate the response, respectively, in the circumferential and longitudinal directions. *Solid line* is the best fit using the isotropic constitutive law (39). Experimental data are from Vande Geest et al. (2006a)

to a particular configuration. For example, when a residual stress arises the natural configuration changes and the material response relative to a different reference configuration in general has a symmetry different from that relative to the original natural configuration.

Ogden and Schulze-Bauer (2000) have shown that residual stresses and collagen fibers in the arterial wall have an important influence on the overall behavior during extension and inflation and on the stress–strain distribution in general. Following the constitutive framework proposed by Holzapfel et al. (2000), Rodríguez et al. (2008) and Basciano and Kleinstreuer (2009) suggest, amongst many others, an additive strain energy function to include the contributions of the isotropic matrix material and of the two families of collagen fibers. For a detailed discussion and relevant references on anisotropic behavior, residual stresses and their correlation to structural constituents within the arterial wall we refer to Humphrey (2001).

The assumption of isotropy in the reference configuration and during inflation is in general untenable. However, we believe that using an isotropic constitutive law does not limit or restrict the main objective of this study, which is to show that experimentally determined pressure loads can be used to determine the wall stresses in a patient-specific aneurysm model. Importantly, also note that inconsistent results have been obtained using an anisotropic constitutive relation to evaluate the stress distribution in patient-specific aortic aneurysms models (Vande Geest et al. 2008).

Another limitation of this analysis is the assumption of a stress free reference configuration. However, since no experimental data are currently available to characterize the magnitude and directions of residual stresses in an aneurysmal abdominal aorta, we did not include such an option in the constitutive formulation. For a more detailed discussion on this subject, we refer to Rodríguez et al. (2008). Once, however, additional data become available, it is a straight forward exercise to modify the constitutive law.

5 Numerical analysis

5.1 Model parameters

The material parameters μ and α in the strain energy function (25) need to be determined based on available experimental data. To the best of our knowledge, the only set of data is by Vande Geest et al. (2006a), where planar biaxial extension tests are performed on a total of 26 AAA specimens and 8 age-matched healthy abdominal aortic samples. Data from aneurysmal specimens show an increased stiffness and a reduced extensibility and a higher degree of anisotropy compared to non-aneurysmal tissues, see Fig. 7. Unfortunately, no other experimental data on the nonlinear response of aneurysmal aortic specimens, with which to compare constitutive theories are available at present. In particular, not sufficient data are available to fully characterize the anisotropic elastic properties. For this reason we have restricted attention to a very simple material model, which merely forms a starting point for further developments.

Vande Geest et al. (2006a) use square specimens cut with the edges parallel to the longitudinal and circumferential orientations of the artery and labeled these directions using subscripts $_{ZZ}$ and $_{\Theta\Theta}$, respectively. All stress–strain data are reported as second Piola–Kirchhoff stress $\mathbf{P}$ versus Green–Lagrange strain $\mathbf{E}$. For incompressible material the second Piola–Kirchhoff stress $\mathbf{P}$ is related to the nominal stress by

$$\mathbf{P} = \mathbf{S}\mathbf{F}^{-\mathrm{T}}, \tag{34}$$

and the strain tensor $\mathbf{E}$ is defined as

$$\mathbf{E} = \frac{1}{2}(\mathbf{F}^{\mathrm{T}}\mathbf{F} - \mathbf{I}). \tag{35}$$

Following Vande Geest et al. (2006a), we denote by λ_Θ and λ_Z the principal stretches, respectively, in the circumferential and axial directions. The in-plane Green–Lagrange

components are then given by

$$E_{\Theta\Theta} = \frac{1}{2}(\lambda_\Theta^2 - 1), \quad E_{ZZ} = \frac{1}{2}(\lambda_Z^2 - 1). \tag{36}$$

The Biot (or nominal) stress components in each direction are calculated as

$$t_\Theta = \frac{f_\Theta}{HL_Z}, \quad t_Z = \frac{f_Z}{HL_\Theta}, \tag{37}$$

where f_Θ and f_Z are the measured loads, H the average thickness and L_Θ and L_Z the dimensions of the specimen in the circumferential and longitudinal directions, all determined in the unloaded reference configuration.

To determine the model parameters and to compare the numerical results to the experimental equi-biaxial data by Vande Geest et al. (2006a), we write the components of the second Piola–Kirchhoff stress tensor as

$$\begin{aligned} P_{\Theta\Theta} &= \lambda_\Theta^{-1} t_\Theta = \mu(1 - \lambda_\Theta^{-4}\lambda_Z^{-2}) \exp[\alpha(I_1 - 3)], \\ P_{ZZ} &= \lambda_Z^{-1} t_Z = \mu(1 - \lambda_\Theta^{-2}\lambda_Z^{-4}) \exp[\alpha(I_1 - 3)], \end{aligned} \tag{38}$$

where Eqs. (21), (31) and (34) have been used. As discussed above, the preliminary analysis here considered assumes an isotropic elastic material and restricts attention to the equi-biaxial data. This allows to introduce the notations $\lambda = \lambda_\Theta = \lambda_Z$ and $P = P_{\Theta\Theta} = P_{ZZ}$ and Eqs. (38) reduce to the single constitutive formulation

$$P = \mu(1 - \lambda^{-6}) \exp[\alpha(I_1 - 3)], \tag{39}$$

with $I_1 = 2\lambda^2 + \lambda^{-4}$.

Planar equi-biaxial extension data are extracted from the article of Vande Geest et al. (2006a) and used to determine the two material parameters α and μ in Eq. (39). Using $\mu = 2.5$ kPa and $\alpha = 43.5$ most accurately reproduces the experimental data of the healthy abdominal aortic specimens, see left graph in Fig. 7. The equi-biaxial data of the AAA specimen show a high degree of anisotropy and an anisotropic model is required to account for it. This implies many more material model parameters and, therefore for this initial analysis, we restrict attention to isotropy. The model (39) with $\mu = 1.04$ kPa and $\alpha = 150$ has been used to produce the numerical data shown by the solid line on the right in Fig. 7.

6 Finite element model

The constitutive law discussed in the earlier section has been implemented as a user-defined material (user-subroutine UMAT) utilizing the commercial finite element software package, ABAQUS/Standard (2007). The subroutine UMAT must contain instructions on how to evaluate the components of the Cauchy stress tensor and the tangent stiffness tensor. Such a computational environment is obviously needed to solve boundary value problems in a full three-dimensional setting and involving stress and deformation states that are generally non-uniform. In is convenient to adopt a multiplicative decomposition of the deformation gradient tensor into volumetric and deviatoric parts and therefore the material response is, in general, no longer considered incompressible. In this paper, we do not provide information on the computational framework that is utilized to implement the constitutive model in the context of a nonlinear finite element solution procedure. We refer to Holzapfel et al. (2000) and Bose and Dorfmann (2009) for a detailed discussion on the implementation process of isotropic and anisotropic material models.

The numerical implementation of the constitutive law was first validated and verified by reproducing the analytically obtained equi-biaxial stress-deformation data shown in Fig. 7. As expected, there are very small differences between the two sets of results due to the incompressibility constrained employed in Eq. (39) and the isochoric and volumetric decomposition in UMAT.

Two sets of calculations were performed. The first was a test case to verify the computational approach, using a straight, non-bulged tube loaded with a uniform internal pressure of 16 kPa. The second was the experimental case, in which the patient-based model was loaded with the non-uniform pressure distribution shown in Fig. 6. In each case, wall thickness was assumed to be uniform and was set at 2 mm and the outer diameter at the model entrance was set at 25.4 mm.

The boundary conditions, for the straight tube model, restrained the longitudinal displacement component on each of the two end sections and left all remaining displacement degrees of freedom unrestrained. It is also well known that eight-node hexahedron elements do not have rotation degrees of freedom and are therefore not effective in modeling bending. To account for the bending stiffness we performed grid independency studies and found that four elements through the wall thickness are necessary.

The geometric layout of the patient-based AAA model, shown in Fig. 1, was used to build the finite element model in Fig. 3. The computational model uses a total of 63,654 elements connected at 127,926 nodes. This results into 383,778 degrees of freedom. The applied boundary conditions restrained all displacement degrees of freedom on each of the two cross-sectional boundary surfaces. These conditions create artificially high stress concentrations at the edges but do not influence the results in the zone of interest. The pressure applied to the inner surface was uniform in the circumferential direction and varied longitudinally as shown in Fig. 6. In both calculations, the outer surfaces of the models were traction free.

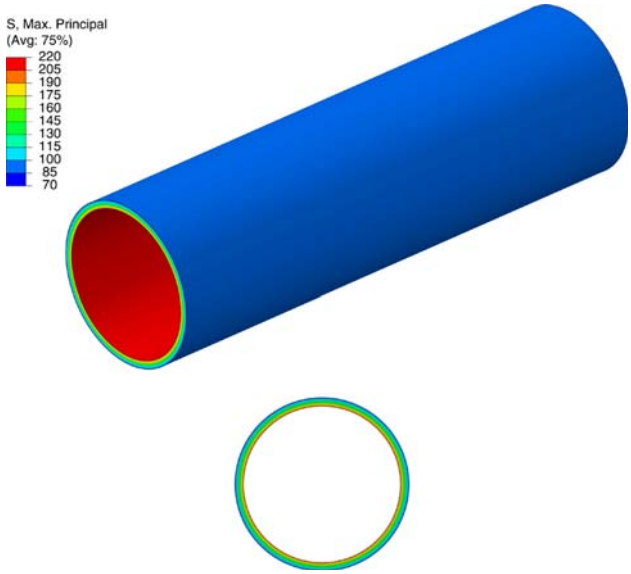

Fig. 8 Axisymmetric distribution of the maximum principal stress in a straight non-bulged tube with constant pressure of 16 kPa applied to the inner surface

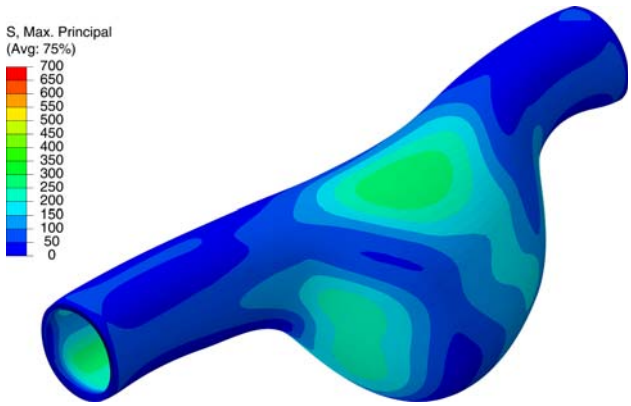

Fig. 9 Highly non-uniform maximum principal stress distribution on the outer surface of the patient-specific AAA model. The pressure applied to the inner surface is uniform in the circumferential direction and varies longitudinally, the outer surface is traction free

6.1 Results

The maximum principal stress distribution for the straight tube is shown in Fig. 8 and for the patient-based AAA model in Figs. 9 and 10. As expected, the results for the straight tube show a uniform and axisymmetric distribution of max principal wall stresses. In particular, the magnitude of the principal stress is largest on the inner surface equal to 220 kPa. Between the inner and outer surfaces, the value of the maximum principal stress decreases monotonically with radial position and reduces to its minimum of 97.9 kPa.

The principal stress distribution in the patient-based model, shown in Figs. 9 and 10, is much more complex than

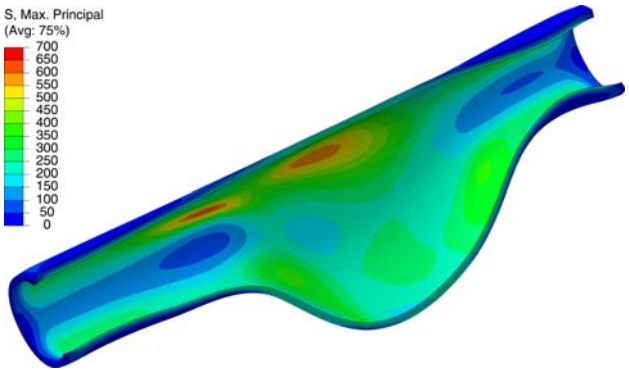

Fig. 10 Maximum principal stress distribution on the inner surface of the patient-specific AAA model. Regions of high stress concentration of approximately 660 kPa are visible on the posterior side of the wall

the straight tube. The magnitude of the stress on the outer surface is relatively small, but not uniform over the whole model, varying from 50 kPa both proximal and distal to the bulge to approximately 400 kPa on the posterolateral surface. Stress on the inner surface of the anterior wall, along the bulge, is also relatively low. However, localized regions of elevated stress form on the inner surface of the posterior side of the wall, both at the proximal neck and at the mid-bulge, with a maximum value of 660 kPa.

7 Discussion

The goal of this study was to use a patient-specific geometry to first experimentally determine the non-uniform distribution of wall pressure produced by steady flow, and then use this pressure distribution as a loading condition to evaluate the associated wall stress field. It has been shown by several authors that aortic aneurysm simulations based on simplified, idealized geometries approximating the shape of patient lesions do not accurately evaluate the wall stress distribution (Mower 1993; Elger et al. 1996; Hua and Mower 2001; Stringfellow et al. 1987). A general agreement has developed that accurate representation of the wall geometry taking into consideration the complex variation of its curvatures is essential for meaningful analysis of wall stress as emphasized, for example, by Vorp (2007) and Watton and Hill (2009). Accordingly, our analysis reproduced the patient wall and lumen geometry. Flow field measurements were performed at Reynolds numbers dynamically emulating in vivo flow conditions, and the wall material properties and constitutive law were selected to reflect patient-average aneurysmal properties.

Physiologically correct representation of these patient features can alter predictions of both wall stress magnitude and wall stress distribution significantly. For example,

Vorp et al. (1998) report that maximum wall stress in idealized, smoothly curved models occur on the posterior wall for bulges of <5 cm maximum diameter, but migrate to the anterior wall for lesions with larger diameters. In contrast, the patient-based lesion studied here showed maximum stress on the posterior wall even though maximum diameter was 5.6 cm.

Oddly, the small region of near maximum principal stress on the posterior wall in the mid-bulge occurred in a region for which the wall pressure had its smallest magnitude as shown in Fig. 6. Clearly, this locally elevated stress region resulted from the combined effects of the pressure distribution, the wall curvature and the wall elasticity. Although autopsy studies have not shown any one particular region of the AAA wall to be a predominant site of rupture, it is interesting to note that failure along the posterior wall has been reported to occur more frequently than failure at other sites (Darling et al. 1977). The actual likelihood of any individual aneurysm failing at a specific location can be expected to depend on both the wall stress and its strength at that position. We refer to Vande Geest et al. (2006b) for a statistical model to estimate the wall strength and its spatial distribution. In our calculation, the maximum principal stress occurred at the proximal bulge neck. However, wall strength in the neck region has been suggested to be greater than strength in the bulge (Vorp et al. 1998). Consequently, it is possible that failure would be most probable in the dilated bulge, if relatively high stresses occurred in the bulge, even if higher stresses occurred in the neck. Thus the elevated stress region found on the mid-bulge posterior inner surface in our calculation may credibly be associated with a position at which the aneurysm is potentially at risk of failure. This correspondence suggests the plausibility of our calculations.

To our knowledge, the experiments and calculations presented here are the first attempt to develop a wall stress analysis incorporating non-uniform pressure reflecting in vivo physiologic conditions. As such, a number of assumptions were made to simplify the calculations. First the patient studied was selected specifically for the smoothly varying, relatively uniform curvature of its lesion, to minimize the difficulty of fabricating the phantom and measuring its wall pressure distribution and to maximize the likelihood of obtaining converged wall stress results. As a result, though, its wall pressure distribution was comparatively uniform, which minimized the deviation of the maximum principal stress from that calculated under a uniform loading assumption. A control calculation applying uniform load to this patient geometry produced only small differences in maximum stress magnitude and location from the non-uniformly loaded model. However, such small differences would not be expected to be representative of the results when more significantly non-uniform loading is combined with spatially varying wall curvature and non-uniform wall thickness.

Second, it was assumed that the wall pressure varied only in the stream-wise direction, and was uniformly distributed circumferentially around the lesion wall. Third, although aneurysmal lesions present significantly anisotropic material properties in vivo, here an average of the axial and circumferential stress–stress data reported by Vande Geest et al. (2005) and Vande Geest et al. (2008) was used to represent a single isotropic behavior. In addition, the wall was assumed to be homogeneous with constant thickness. In fact, AAAs in vivo show localized calcification deposits that create material inhomogeneities, and generally have spatially varying, non-uniform wall thickness. Each of these simplifications would be expected to minimize wall stress non-uniformity and possibly limit maximum wall stress development in the calculation. Finally flow-induced wall shear stresses, which were found to be five to six orders of magnitude less than wall normal stress by direct measurements (Edgar 2008), were neglected in computing wall internal stress. All of these assumptions can be improved in future studies. We are currently in the process of developing non-axially symmetric pressure measurements that will be used as part of a forthcoming analysis. We also plan studies under pulsatile flow conditions emulating unsteady in vivo waveforms in both rest and exercise, with more anatomically realistic models incorporating major aortic branch vessels, and we plan to introduce anisotropic material properties and non-uniform wall thickness to our analysis. However, our goal at this initial stage of the project was primarily to develop the methodology.

As best we can determine, the only experimental measurements of wall pressure distribution in patient-based phantoms reported to date are the data presented here. At high Reynolds numbers, flow field turbulence produced strong fluctuations of the wall pressure signal, with instantaneous bursts an order of magnitude greater than the pressure signal standard deviation. Since those brief bursts can significantly amplify wall pressure spatial gradients while they are present, they would be expected to strongly increase the flow-induced wall stress magnitude. Accordingly, it would be of interest to investigate the relations between turbulence, wall pressure fluctuations and patient lesion geometry. Comparison of our results with those of such a study would allow rigorous evaluation of the generality of turbulence effects on wall pressure and the importance of turbulence in wall stress development.

The values of maximum principal stress reported here are of the same order as corresponding stresses reported by other authors studying wall stress under the assumption of uniform wall pressure (Vorp 2007). However, our analysis produced a notably greater maximum stress magnitude. Stresses in straight tube test cases reported in Raghavan et al. (2000) and Vorp (2007) were similar to those found here, suggesting that the different computational approaches used here and by those authors would lead to comparable results when applied to similar geometries. However, Raghavan et al. (2000) show

the magnitude of the highest principal stress in their patient-based study to vary from 290 to 450 kPa depending on the geometric layout and dimensions of the model. Wang et al. (2002) found maximum von Mises stress values in the same range. In contrast, the maximum principal stress in the patient-based model in our analysis was 660 kPa. This is an interesting and potentially significant difference, since Raghavan et al. (2000) reported failure strength of patient-specific wall tissue samples to decrease from 1,210 kPa in a non-aneurysmal aorta to 650 kPa in an aneurysmal vessel. Thus the effect of non-uniform loading on maximum wall stress development may be a clinically important issue. Future analyses will address the effects of wall pressure and wall material non-uniformities on AAA stress development.

8 Concluding remarks

In summary, maximum principal stress distribution in a finite element model of a patient aortic aneurysm has been evaluated. A physiologically based method for calculating wall stress using experimentally measured pressure data from a corresponding phantom as loading has been developed and successfully implemented. The method predicts a complex distribution of wall stress, with maximum magnitude on the posterior surface of aneurysmal bulge, a position that has been suggested to be a common site of rupture. The analysis also predicts a similar order of magnitude for maximum stress as reported by other authors under the assumption of uniform internal loading. However, a significantly larger maximum principal stress is predicted, 660 versus 400–450 kPa. This is potentially very significant, since measurements of aneurysmal tensile strength reported by other authors were 650 kPa. Future studies will address the limitations of the model described above.

Acknowledgments This project was partially supported by NSF award CBET-0733498. The authors wish to thank Ms. Elham Aslani for assistance with segmentation of the CT images and preparation of the vessel models.

References

ABAQUS V6.7 (2007) Dassault Systèmes Simulia. ABAQUS, Providence

Asbury CL, Ruberti JW, Bluth EI, Peattie RA (1995) Experimental investigation of steady flow in rigid models of abdominal aorticaneurysms. Ann Biomed Eng 23:29–39

Ashton HA, Buxton MJ, Day NE, Kim LG, Marteau TM, Scott RA, Thompson SG, Walker NM (2002) The multicentre aneurysm screening study (MASS) into the effect of abdominal aortic aneurysm screening on mortality in men: a randomized control trial. Lancet 360:1531–1539

Basciano CA, Kleinstreuer C (2009) Invariant-based anisotropic constitutive models of the healthy and aneurysmal abdominal aortic wall. ASME J Biomech Eng 131:021009

Bluestein D, Dumont K, De Beule M, Ricotta J, Impellizzeri P, Verhegghe B, Verdonck P (2009) Intraluminal thrombus and risk of rupture in patient specific abdominal aortic aneurysms—FSI modeling. Comput Methods Biomech Biomed Eng 12:73–81

Bluth EI, Murphey SM, Hollier LH, Sullivan MA (1990) Color flow doppler in the evaluation of aortic aneurysms. Int Angiol 9:8–10

Bose K, Dorfmann A (2009) Computational aspects of a pseudo-elastic constitutive model for muscle properties in a soft-bodied arthropod. Int J Nonlinear Mech 44:42–50

Chuong CJ, Fung YC (1984) Compressibility and constitutive equation of arterial-wall in radial compression experiments. J Biomech 17:35–40

Darling RC, Messina CR, Brewster DC, Ottinger LW (1977) Autopsy-study of unoperated abdominal aortic aneurysms. Circulation 56:161–164

Demiray H (1972) Elasticity of soft biological tissues. J Biomech 5:309–311

Edgar ES (2008) Computational and experimental investigation of steady flow fields, turbulence and hemodynamic wall stresses in patient-specific abdominal aortic aneurysm models. M.S. Thesis, Oregon State University

Elger DF, Blackketter DM, Budwig RS, Johansen KH (1996) The influence of shape on the stresses in model abdominal aorticaneurysms. ASME J Biomech Eng 118:326–332

Fillinger M (2006) The long-term relationship of wall stress to the natural history of abdominal aortic aneurysms (finite element analysis and other methods). Ann N Y Acad Sci 1085:22–28

Fung YC (1981) Biomechanics: mechanical properties of living tissue. Springer, New York

Holzapfel GA (2001) Nonlinear solid mechanics: a continuum approach for engineering. Wiley, Chichester

Holzapfel GA, Gasser TC, Ogden RW (2000) A new constitutive framework for arterial wall mechanics and a comparative study of material models. J Elast 61:1–48

Holzapfel GA, Ogden RW (2009) On planar biaxial tests for anisotropic nonlinearly elastic solids. A continuum mechanical framework. Math Mech Solids 14:474–489

Hua J, Mower WR (2001) Simple geometric characteristics fail to reliably predict abdominal aortic aneurysm wall stresses. J Vasc Surg 34:308–315

Humphrey JD (2001) Cardiovascular solid mechanics cells tissues and organs. Springer, New York

Humphrey JD, Taylor CA (2008) Intracranial and abdominal aorticaneurysms: similarities, differences, and need for a new class of computational models. Annu Rev Biomed Eng 10:221–246

Humphrey JD, Yin FCP (1987) A new constitutive formulation for characterizing the mechanical behavior of soft tissues. Biophys J 52:563–570

Johansson G, Swedenborg J (1986) Ruptured abdominal aortic aneurysms: a study of incidence and mortality. Br J Surg 73:101–103

Li Z, Kleinstreuer C (2006) Effects of blood flow and vessel geometry on wall stress and rupture risk of abdominal aorticaneurysms. J Med Eng Technol 30:283–297

Li ZY, U-Ying-Im J, Tang TY, Soh E, See TC, Gillard JH (2008) Impact of calcification and intraluminal thrombus on the computed wall stresses of an abdominal aortic aneurysm. J Vasc Surg 47:928–935

Lin HT, Dorfmann AL, Trimmer BA (2009) Soft cuticle biomechanics: a constitutive model of anisotropy for caterpillar integument. J Theor Biol 256:447–457

Mower WR, Baraff LJ, Sneyd J (1993) Stress distributions in vascular aneurysms—factors affecting risk of aneurysm rupture. J Surg Res 55:155–161

Nevitt MP, Ballard DJ, Hallett JW (1989) Prognosis of abdominal aortic aneurysms: a population based study. New Engl J Med 321:1009–1014

Newman AB, Arnold AM, Burke GL, O'Leary DH, Manolio TA (2001) Cardiovascular disease and mortality in older adults with small abdominal aortic aneurysms detected by ultrasonography: the cardiovascular health study. Ann Intern Med 134:182–190

Ogden RW (1997) Nonlinear elastic deformations. Dover, New York

Ogden RW, Schulze-Bauer CAJ (2000) Phenomenological and structural aspects of the mechanical response of arteries (with C. A. J. Schulze-Bauer). In: Casey J, Bao G (eds) Mechanics in biology. ASME AMD-Vol. 242/BED-Vol. 46:125–140

O'Rourke MJ, McCullough JP (2008) A comparison of the measured and predicted flowfield in a patient-specific model of an abdominal aortic aneurysm. Proc Inst Mech Eng Part H J Eng Med 222:737–750

Papaharilaou Y, Ekaterinaris JA, Manousaki E, Katsamouris AN (2007) A decoupled fluid structure approach for estimating wall stress in abdominal aortic aneurysms. J Biomech 40:367–377

Peattie RA, Asbury CL, Bluth EI, Ruberti JW (1996a) Steady flow in models of abdominal aortic aneurysms. Part I: investigation of the velocity patterns. J Ultrasound Med 15:679–688

Peattie RA, Asbury CL, Bluth EI, Riehle TJ (1996b) Steady flow in models of abdominal aortic aneurysms. Part II: wall stresses and their implications for in vivo thrombosis and rupture. J Ultrasound Med 15:689–696

Peattie RA, Riehle TJ, Bluth EI (2004) Pulsatile flow in fusiform models of abdominal aortic aneurysms: flow fields, velocity patterns and wall stresses. ASME J Biomech Eng 126:438–446

Raghavan ML, Vorp DA (2000) Toward a biomechanical tool to evaluate rupture potential of abdominal aortic aneurysms: identification of a finite strain constitutive model and evaluation of its applicability. J Biomech 33:475–482

Raghavan ML, Vorp DA, Federle MP, Makaroun MS, Webster MW (2000) Wall stress distribution on three-dimensionally reconstructed models of human abdominal aortic aneurysm. J Vasc Surg 31:760–769

Rissland P, Alemu Y, Einav S, Ricotta J, Bluestein D (2009) Abdominal aortic aneurysm risk of rupture-patient specific FSI simulations using anisotropic model. J Biomech Eng 131:031001–031010

Rodríguez JF, Ruiz C, Doblare M, Holzapfel GA (2008) Mechanical stresses in abdominal aortic aneurysms: influence of diameter, asymmetry, and material anisotropy. ASME J Biomech Eng 130:021023

Scotti CM, Jimenez J, Muluk SC, Finol EA (2008) Wall stress and flow dynamics in abdominal aortic aneurysms: finite element analysis vs fluid-structure interaction. Comput Methods Biomech Biomed Eng 11:301–322

Singh K, Bønaa KH, Jacobsen BK, Bjørk L, Solberg S (2001) Prevalence of and risk factors for abdominal aortic aneurysms in a population-based study: the Tromsø study. Am J Epidemiol 154:236–244

Speelman L, Bohra A, Bosboom EMH, Schurink GW, Van de Vosse FN, Makaroun MS, Vorp DA (2007) Effects of wall calcifications in patient-specific wall stress analyzes of abdominal aortic aneurysms. ASME J Biomech Eng 129:105–109

Stringfellow MM, Lawrence PF, Stringfellow RG (1987) The influence of aorta aneurysm geometry upon stress in the aneurysm wall. J Surg Res 42:425–433

Truijers M, Pol JA, Schultzekool LJ, van Sterkenburg SM, Fillinger MF, Blankensteijn JD (2007) Wall stress analysis in small asymptomatic, symptomatic and ruptured abdominal aortic aneurysms. Eur J Vasc Endovasc 33:401–407

Vande Geest JP (2005) Towards an improved rupture potential index for abdominal aortic aneurysms: anisotropic constitutive modeling and noninvasive wall strength estimation. PhD Thesis, University of Pittsburgh

Vande Geest JP, Bohra A, Sun W, Di Martino E, Sacks MS, Vorp DA (2004) Development and 3D finite element implementation of a multiaxial constitutive relation for abdominal aortic aneurysms. In: Proceedings of the international mechanical engineering conference

Vande Geest JP, Sacks MS, Vorp DA (2006a) The effects of aneurysm on the biaxial mechanical behavior of human abdominal aorta. J Biomech 39:1324–1334

Vande Geest JP, Wang DH, Wisniewski SR, Makaroun MS, Vorp DA (2006b) Towards a noninvasive method for determination of patient-specific wall strength distribution in abdominal aortican-eurysms. Ann Biomed Eng 34:1098–1106

Vande Geest JP, Schmidt DE, Sacks MS, Vorp DA (2008) The effects of anisotropy on the stress analyzes of patient-specific abdominal aortic aneurysms. Ann Biomed Eng 36:921–932

Vorp DA (2007) Review: biomechanics of abdominal aortic aneurysm. J Biomech 40:1887–1902

Vorp DA, Raghavan ML, Webster MW (1998) Mechanical wall stress in abdominal aortic aneurysm: influence of diameter and asymmetry. J Vasc Surg 27:632–639

Wang DHJ, Makaroun MS, Webster MW, Vorp DA (2002) Effect of intraluminal thrombus on wall stress in patient-specific models of abdominal aortic aneurysm. J Vasc Surg 36:598–604

Watton PN, Hill NA (2009) Evolving mechanical properties of a model of abdominal aortic aneurysm. Biomech Model Mechanobiol 8:25–42